

## Design of a high temperature (1350 °C) solar receiver based on a liquid metal heat transfer fluid: Sensitivity analysis

Freddy DeAngelis<sup>a</sup>, Hamid Reza Seyf<sup>a</sup>, Rebecca Berman<sup>b</sup>, Greg Schmidt<sup>b</sup>, Duncan Moore<sup>b</sup>, Asegun Henry<sup>c,\*</sup>

<sup>a</sup> George W. Woodruff School of Mechanical Engineering, Georgia Institute of Technology, 801 Ferst Drive, Atlanta, GA 30302, United States

<sup>b</sup> Institute of Optics, University of Rochester, Rochester, NY 14620, United States

<sup>c</sup> George W. Woodruff School of Mechanical Engineering, School of Materials Science and Engineering, Heat Lab, Georgia Institute of Technology, 801 Ferst Drive, Atlanta, GA 30302, United States

### ARTICLE INFO

#### Keywords:

Liquid metal  
Solar thermal  
Receiver  
Efficiency

### ABSTRACT

One approach to reducing the cost of concentrated solar power is to improve the heat engine efficiency by increasing its maximum operating temperature. To achieve higher operating temperatures, we have studied using a liquid metal heat transfer fluid in conjunction with a receiver made from a ceramic/refractory material. As a first step in the design of such a receiver, we conducted sensitivity analyses of several receivers, allowing us to determine what factors most significantly affect receiver performance. Material properties, natural convection from the receiver cavity, and the location of hot spots within the cavity were found to have the largest effect on receiver efficiency. It was also determined that stresses due to thermal expansion can exceed the fracture strength of the receiver material if care is not taken to minimize these stresses. Interestingly, the stress as opposed to performance considerations, set the most important constraints on the receiver geometry.

### 1. Introduction

Considering the imminent effects of climate change (Pachauri et al., 2014), developing a carbon-neutral approach to electricity is becoming an ever increasing priority. Although many renewable technologies, such as wind and photovoltaics (PV), have experienced major reductions in their levelized cost of energy (LCOE) (Branz et al., 2015; Donohoo-Vallett, 2016), it has now become clear that finding an inexpensive way to dispatchably store energy is critical (Denholm et al., 2016, 2013; Denholm and Mehos, 2014; Sioshansi et al., 2014). Concentrated solar power (CSP) with thermal energy storage (TES) is currently the most cost effective option, but it is still too expensive, as it currently costs about twice that of new installations of natural gas combined cycle plants (EIA, 2013; NREL, 2016). While there exist several avenues to reducing CSP costs (Pitz-Paal et al., 2005), one of the best opportunities for cost reduction is improving the efficiency of the plant, particularly by increasing the hot side temperature of the power block from 565 °C to temperatures high enough to allow for a Brayton-Rankine combined cycle to be used (i.e. > ~1000 °C); doing so can increase the power block efficiency by upwards of 50% (Rolf et al., 1999).

#### 1.1. Material selection for high-temperature CSP

Current state of the art CSP utilizes molten nitrate salts as the HTF and stainless steel or, in some cases, nickel alloys as the containment material (Fernandez et al., 2012; Goods and Bradshaw, 2004). To achieve temperatures necessary for a combined cycle however, refractory materials not found in current CSP plants must be used. Finding a suitable HTF to use in a CSP plant is one of the primary limitations that prevents CSP from attaining extreme temperatures and is problematic for a number of reasons (Becker et al., 2006; Bertocchi, 2002; Bradshaw and Meeker, 1990; Bradshaw and Siegel, 2008; Bugge et al., 2006; Cable et al., 2003; Fernandez et al., 2012; Garcia-Casals and Ajona, 1999; Goods and Bradshaw, 2004; Karni et al., 1997, 1998; Kribus et al., 1999; Kruienza and Gill, 2014; Margolis et al., 2012; Pitz-Paal et al., 1997; Ries et al., 1997; Ries and Spirkel, 1996; Siegel et al., 2010; Weitzel, 2011; Wright et al., 2004). To overcome the issues presented by other heat transfer media, a liquid metal heat transfer fluid (LMHTF) is considered herein for use in a power tower receiver. LMHTF's have many properties that make them desirable for use at extreme temperatures (Pacio and Wetzel, 2013; Yang and Garimella,

*Abbreviations:* PV, photovoltaic; LCOE, levelized cost of electricity; CSP, concentrated solar power; TES, thermal energy storage; TIT, turbine inlet temperature; LMHTF, liquid metal heat transfer fluid; MCRT, Monte Carlo ray tracing; HFSS, high flux solar simulator; CFD, computational fluid dynamics

\* Corresponding author.

E-mail addresses: [adeangelis3@gatech.edu](mailto:adeangelis3@gatech.edu) (F. DeAngelis), [ase@gatech.edu](mailto:ase@gatech.edu) (A. Henry).

<https://doi.org/10.1016/j.solener.2018.02.040>

Received 27 March 2017; Received in revised form 8 February 2018; Accepted 13 February 2018

Available online 14 March 2018

0038-092X/ © 2018 Elsevier Ltd. All rights reserved.

**Nomenclature**

$A$	area (m <sup>2</sup> )	$T$	temperature (K)
$C_p$	specific heat capacity (J kg <sup>-1</sup> K <sup>-1</sup> )	$u$	fluid velocity (m/s)
$E$	Young's modulus (Pa)	$\alpha$	thermal expansion coefficient
$F$	view factor	$\varepsilon$	radiative emissivity
$g$	gravitational acceleration (m s <sup>-1</sup> )	$\varepsilon$	strain
$h$	convective heat transfer coefficient (W m <sup>-2</sup> K <sup>-1</sup> )	$\eta$	efficiency
$k$	thermal conductivity (W m <sup>-1</sup> K <sup>-1</sup> )	$\mu$	dynamic viscosity (kg m <sup>-1</sup> s <sup>-1</sup> )
$\dot{m}$	mass flowrate (kg s <sup>-1</sup> )	$\rho$	density (kg m <sup>-3</sup> )
$p$	pressure (Pa)	$\sigma$	Stefan-Boltzmann constant (W m <sup>-2</sup> K <sup>-4</sup> )
$q''$	heat flux (W m <sup>-2</sup> )	$\sigma$	stress (Pa)
$R$	thermal resistance (K W <sup>-1</sup> )	$\Phi$	viscous forces term of Navier-Stokes equations
		$\phi$	flux (W m <sup>-2</sup> )

2010), particularly their high thermal conductivity and the large temperature range over which they remain liquid. Several LMHTF candidates for CSP exist; however, few are liquid in the temperature range of interest and unreactive/non-toxic enough in liquid form to use safely, and even fewer are economically feasible in a large-scale plant. Nevertheless, we have identified two LMHTF's as candidates for use in high-temperature CSP applications (Wilk, 2016), namely aluminum-silicon (Al-Si) alloys and tin (Sn). We limit our sensitivity analysis here to the latter. Graphite is used as the containment material, as it is a refractory that does not form compounds with Sn and thus, it can be used to make an entire system without any corrosion whatsoever (Amy et al., 2017; Zhang et al., 2018); mullite was considered for similar reasons, but was not used in later receiver designs. Furthermore, a recent demonstration of an all ceramic pump operating at 1200 °C, pumping liquid tin, has opened up the potential for a new version of CSP that leverages such a refractory based infrastructure.

### 1.2. Receiver design for high-temperature CSP

While most existing commercial plants employ external receivers, at the extreme temperatures of interest (i.e., > 1000 °C), an external receiver would lose too much heat through reradiation to yield a net gain in overall system efficiency. Thus a cavity design is necessary to construct a high-efficiency receiver, to limit the view factor of the receiver to the surroundings. The present investigation is a first step to reducing losses from a receiver assembly. Here, we perform a sensitivity analysis to identify the most important design parameters and attempt to answer the question of whether an efficient (~90%) receiver can be realized at temperatures > 1000 °C. Here, the receiver efficiency,  $\eta$ , is defined as

$$\eta = \frac{\int_{T_{inlet}}^{T_{outlet}} \dot{m} C_p(T) dT}{\int \phi(r, \theta, z) dA} \quad (1)$$

where  $T_{inlet}$  is the inlet temperature of the HTF,  $T_{outlet}$  is the average outlet temperature of the HTF,  $\dot{m}$  is the mass flow rate of the HTF,  $C_p(T)$  is the specific heat of the HTF as a function of temperature,  $\phi(r, \theta, z)$  is the spatially dependent radiant flux entering the cavity through an aperture, given in kW m<sup>-2</sup>, and  $A$  is the area of the aperture.

Cavity receiver efficiency is fundamentally limited by its reradiation. Steinfeld provides an expression for the theoretical maximum efficiency of a cavity receiver, by assuming the only loss is reradiation through the aperture, via (Steinfeld, 2002)

$$\eta_{max} = 1 - \frac{\sigma T^4}{\phi} \quad (2)$$

where  $\sigma$  is the Stefan-Boltzmann constant,  $T$  is the nominal blackbody temperature of the receiver, and  $\phi$  is the average flux of light coming through the receiver aperture.

Not only do thermal losses increase at higher temperatures, but thermal stresses in the receiver also become more significant. Furthermore, even though it possesses superior thermal shock

resistance, graphite has a low fracture strength (~50 MPa), and a critical stress intensity factor,  $K_{Ic}$ , of only ~1 MPa-√m (Rose, 1985). Thus, it is not clear without first calculating the temperature distribution that the thermal stresses will not exceed the limits of the candidate material. Therefore, it is necessary to model the system to calculate expected temperature profiles so that subsequent stress analyses and efficiencies can be evaluated for feasibility.

Here, we attempt to analyze a small-scale receiver as an important first step towards determining what factors must be considered at larger scales. Although one can qualitatively predict *a priori* what types of materials and system properties are likely to yield the best performance, it is not clear if the properties that can be realized with commercially available materials are sufficient to allow for actual testing without immediate failure, or whether such materials are even sufficient to reach the nominal target of 90% efficiency after optimization. Among the most significant questions associated with the design of such a receiver are the following:

- The difference between the inlet and outlet temperatures of the receiver is on the order of 1000 °C, and the thermal conductivity of graphite changes by nearly an order of magnitude over this temperature range. Is graphite sufficiently thermally conductive, such that it does not form hot spots leading to substantial reradiation from the cavity or thermal stresses in excess of graphite's fracture strength?
- To construct an efficient receiver, thermal losses must be quantified. Radiation and convection from the cavity aperture as well as off the surfaces of the insulation are primary loss mechanisms, but it is not clear *a priori* which loss mechanisms will dominate, or which options are available to mitigate such losses.
- The radiative heat flux on different parts of a cavity receiver can potentially vary by orders of magnitude and is highly dependent on receiver geometry. Reradiation depends on the temperature at a given location in the receiver, which is in turn affected by several factors, such as the incident flux at that particular location. Thus, another question is to what extent can the temperature/radiation distribution in the cavity be manipulated to improve efficiency by suppressing reradiation?

In the following sections, we describe a full, steady-state model constructed to evaluate the aforementioned effects and to assess the sensitivity of a receiver to each of these various parameters. The parameters altered include the thermal conductivity and emissivity of both graphite and insulation, dimensions and receiver geometry, LMHTF flowrate, and the value of convective coefficient on both the outer insulation surface and the surfaces inside the receiver cavity.

## 2. Methodology

To create an efficient receiver geometry, a base-case receiver was

first used to evaluate the effects of altering different material properties. The receiver geometry itself was then altered and iterated upon to produce a final receiver design.

Receiver geometry was considered with three primary design criteria: (1) minimize the chance of receiver failure due to effects such as thermal stresses, (2) maximize the conversion efficiency from sunlight to thermal energy, and (3) maintain a liquid metal outflow temperature of at least 1350 °C (chosen because it allows for the use of SiC that might have residual Si, which melts at 1414 °C).

In our receiver designs, the receivers use an inner layer of high temperature zirconia insulation capable of withstanding temperatures in excess of 1500 °C (1). The zirconia is surrounded by microporous insulation that can operate at temperatures up to 1000 °C. The thermal conductivities of the two types of insulation vary between 0.2 and 0.5 W m<sup>-1</sup> K<sup>-1</sup> (1) and 0.01–0.05 W m<sup>-1</sup> K<sup>-1</sup> (2) respectively in the simulated temperature range. It should be noted that thermal conductivity data cited here is specific to the bulk insulation used in our experiment. Thus, effects such as, e.g. temperature increasing the thermal conductivity of gas within voids in the insulation, have already been accounted for.

### 2.1. The U-tube receiver geometry (Base Case)

The U-tube receiver (Fig. 1) consists of a cylindrical cavity with a U-shaped pipe within the cavity through which the LMHTF Sn(l) flows. Though not expected to be particularly efficient, the computational time required to simulate this receiver is low due to the simplicity of the fluid velocity profile. Therefore, this receiver geometry was used as a base case to conduct parametric sweeps over different receiver dimensions and material properties, before the geometry itself was optimized.

A number of parameters were varied for the U-tube sensitivity analysis. These parameters include the thermal conductivity and emissivity of various materials, the dimensions of the cavity, and the effective convective coefficient for both the surface of the insulation and the surfaces within the cavity.

### 2.2. The cup-cone receiver geometry

The cup-cone receiver (Fig. 2) consists of two nested “cups”, with Sn flowing between into the receiver at its base and up the side walls, exiting at the top of the walls, near the lid. Light enters an aperture through the “lid” of the cup and is absorbed by the inner cavity. A taper at the inlet region creates a longer flow path, reducing temperature gradient, and therefore thermal stresses; without the tapered inlet, the thermal stresses developed are in excess of graphite’s fracture strength. The receiver lid is made of rigid insulation.

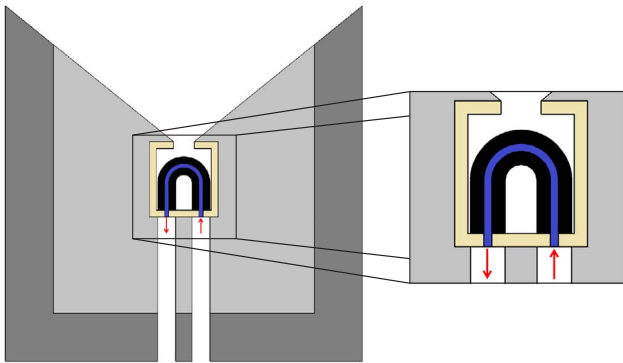


Fig. 1. Cross section of the U-shaped tube receiver. Microporous insulation is shown in dark gray, zirconia in light gray, mullite in beige, graphite in black, and Sn in blue. Direction of Sn flow shown with red arrows. (For interpretation of the references to color in this figure legend, the reader is referred to the web version of this article.)

### 2.3. Model description

To accurately determine the flux profile of the light incident on receiver cavity surfaces, Monte Carlo ray tracing (MCRT) was performed, assuming the high flux solar simulator (HFSS) at the University of Minnesota as the radiant source (Krueger, 2012). The source consists of seven total XBO® 6500 W/HSLA OFR OSRAM lamps arranged in a hexagonal pattern around a central lamp, delivering approximately 9.2 kW to a spot 6 cm in diameter. The flux at the center of this spot is in excess of 7000 kW m<sup>-2</sup>, with an average flux of about 3200 kW m<sup>-2</sup> over the full 6 cm diameter.

The maximum Reynolds number for Sn flowing within any receiver geometry presented here is ~1000, occurring within the U-tube receiver. In the cup-cone receiver, the Reynolds number is < 100 everywhere, so flow was modeled as laminar in all cases. The governing equations for a Newtonian, incompressible, three-dimensional Sn flow inside graphite tubes with temperature dependent viscosity and thermal conductivity are expressed as follows:

Mass continuity:

$$\frac{\partial(\rho u_i)}{\partial x_i} = 0 \tag{3}$$

Momentum continuity:

$$\frac{\partial(u_i \rho u_j)}{\partial x_i} = -\frac{\partial p}{\partial x_i} + \frac{\partial}{\partial x_i} \left( \mu \frac{\partial u_j}{\partial x_i} \right) \tag{4}$$

Energy continuity in the fluid domain is given by:

$$\frac{\partial(\rho C_p u_i T)}{\partial x_i} = \frac{\partial}{\partial x_i} \left( k_f \frac{\partial T}{\partial x_i} \right) + \mu \Phi \tag{5}$$

Energy continuity in the solid domains is expressed as:

$$\frac{\partial}{\partial x_i} \left( k_s \frac{\partial T}{\partial x_i} \right) = 0 \tag{6}$$

where  $u$  is the fluid velocity vector,  $\rho$  is density,  $p$  is pressure,  $\mu$  is the fluid dynamic viscosity,  $C_p$  is the specific heat capacity,  $T$  is temperature, and  $\Phi$  is the dissipation function, which gives the time rate at which energy is dissipated per unit volume due to viscous effects. Here, the Sn is treated as a Newtonian fluid. However, as will be shown later, the results are very insensitive to the fluid dynamics within the Sn.

At the solid-fluid interface, the temperature and heat flux of the solid and fluid were set equal, i.e.,  $k_f \frac{\partial T_f}{\partial n} = k_s \frac{\partial T_s}{\partial n}$  where the subscripts  $s$  and  $f$  denote the solid and fluid, respectively. A constant and uniform velocity and temperature ( $T_{in} = 300$  °C) is applied at the fluid inlet of computational domain. At the outlet, the static pressure is fixed and the remaining flow variables are extrapolated from interior of computational domain, i.e.,  $\frac{\partial u_i}{\partial m} = \frac{\partial T_f}{\partial m} = \frac{\partial T_s}{\partial m} = 0$ , where  $m$  is the vector normal to outlet. The no slip boundary condition is applied at the all internal and external walls.

Surfaces inside the cavity were modeled to exchange radiation with other surfaces inside the cavity as well as the insulation that comprises the aperture and the surrounding environment. These surfaces can also convect directly to the surrounding environment with an effective heat transfer coefficient  $h_{IC}$ . Lastly, these surfaces are externally heated by the light source (e.g., simulated sunlight), with an effective, spatially varying absorbed flux  $q''_{abs}$ , which was determined separately from this model, using MCRT performed using the LightTools software package. Therefore, the following boundary condition was applied to the inner surfaces of the cavity,

$$q''_{abs} = -k \nabla T + h_{IC} (T - T_{inf}) + \sum_i \frac{\sigma (T^4 - T_i^4)}{R_{radiative}} \tag{7}$$

where the first term is the heat conducted away from the inner cavity surface, the second term is heat loss due to convection off the cavity

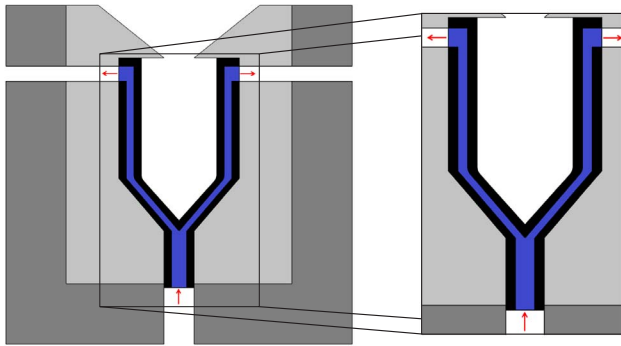


Fig. 2. Cross section of the cup-cone receiver. Microporous insulation is shown in dark gray, zirconia in light gray, graphite in black, and Sn in blue. Direction of Sn flow shown with red arrows. (For interpretation of the references to color in this figure legend, the reader is referred to the web version of this article.)

surface, and the third term is the total radiation exchange between the cavity surface and other radiating surfaces. Here, we have employed the diffuse gray approximation, where  $R_{radiative}$  can be expanded as,

$$R_{radiative,j} = \frac{1-\varepsilon_i}{\varepsilon_i A_i} + \frac{1}{A_i F_{ij}} + \frac{1-\varepsilon_j}{\varepsilon_j A_j} \quad (8)$$

where the index  $i$  denotes the element to which Eq. (7) is being applied. The index  $j$  denotes all other elements with which element  $i$  has a non-zero view factor,  $\varepsilon$  is the material emissivity,  $A$  is the area of the surface element being considered, and  $F_{ij}$  is the view factor between elements  $i$  and  $j$ . All surface to surface radiation that was not associated with the incident sunlight source was modeled using the gray-diffuse approximation, which assumes no preferential direction for re-radiation and is expected to be accurate for the rough graphite surfaces being considered (Wang et al., 2014). All external insulation surfaces experience natural convection and radiation to the surroundings, yielding the following boundary conditions

$$0 = -k\nabla T + h_{OC}(T - T_{inf}) + \sigma\varepsilon(T^4 - T_{amb}^4) \quad (9)$$

where  $h_{OC}$  is the convective coefficient off the outer insulation surface.

Solutions of the governing equations was obtained numerically using the COMSOL Multiphysics software package, employing the finite element method. It is worth noting that because the fluid in question is a liquid metal, the Prandtl number is very low ( $\sim 0.012$  at its melting point (Stewart and Weinberg, 1972; Wolff et al., 1988)). Thus, the heat transfer in the fluid is due primarily to conduction and is largely unaffected by the fluid velocity profile, i.e., any reasonable fluid velocity profile would yield approximately the same temperature profile, as the liquid metal represents a negligible thermal resistance, even in the limit of laminar flow. Numerical solutions to the governing equations using COMSOL are therefore both easily implemented and accurate for the cases considered.

The quantity  $q_{abs}''$  in Eq. (7) was determined by a separate calculation of the absorbed light, using LightTools. Here, since light is non-interacting, incident light has no effect on re-radiated light, and as a result, the absorbed light can be determined separately from the temperature profile. This assumes optical properties are not strongly temperature dependent, which appears to be the case, based on previous measurements (Thorn and Simpson, 1953). Using these assumptions, the absorbed light was first computed in LightTools by MCRT using 1,000,000 rays, based on a CAD model constructed of the HFSS at the University of Minnesota (Krueger, 2012). The model includes the seven Osram xenon arc lamps and their ray data as determined by Zeemax’s Radiant Source Model, with corresponding elliptical mirrors and the receiver.

The absorbed light profile for a given geometry was then imported into COMSOL as a 3D array mapping of heat flux onto the receiver surface using 3D linear interpolation. Aperture size was optimized based on an energy balance to maximize the total net radiation (i.e. radiation entering the cavity minus reradiation).

The natural convective coefficient for the surface of the insulation was calculated based on the relation provided by Incropera for a horizontal cylinder (Bergman et al., 2011) to yield a convective coefficient of  $5.8 \text{ W m}^{-2} \text{ K}^{-1}$ . The emissivity of the insulation was prescribed a nominal value of 0.6 (Tanaka et al., 2001), and the ambient temperature was set to  $25^\circ\text{C}$ . As shown later, the performance of the receivers is insensitive to either of these values.

Solving Eqs. (3)–(9) yielded the temperature profile, which in turn was used to calculate both receiver efficiency (Eq. (1)) and the thermal stresses in the receiver according to

$$\sigma = E[\varepsilon - \alpha(T - T_{ref})] \quad (10)$$

where  $\sigma$  is the total stress in the material,  $E$  is the Young’s modulus,  $\varepsilon$  is the total strain in the material,  $\alpha$  is the coefficient of thermal expansion,  $T$  is the local temperature of the material, and  $T_{ref}$  is the reference temperature at which all thermal stresses are zero ( $25^\circ\text{C}$  in this case).

### 3. Results and discussion

#### 3.1. Mesh convergence

The computational domain was spatially discretized using unstructured grids of tetrahedral volume elements. A fine grid was used in regions with steep velocity and temperature gradient. Three grids of 67,764 (coarse), 288,474 (fine), and 736,263 (very fine) elements were used for the study of grid independency for the U-tube model (see Table 1). Taking the U-Tube receiver as an example, the average fluid velocity, outlet temperature and cavity temperature obtained for the finest mesh (736,263 elements) were within 1% of the fine mesh (288,474 elements). Therefore, the fine mesh was used for subsequent simulations.

Table 1  
Values of parameters examined for different mesh densities. Percent difference between parameters evaluated for fine and finer meshes included.

	Coarse	Fine	Finer	% Difference
Average fluid velocity (m/s)	0.0916	0.0885	0.0885	0.500
Outlet temperature ( $^\circ\text{C}$ )	1768.7	1806.1	1815.5	0.452
Average cavity temperature ( $^\circ\text{C}$ )	1826.2	1861.2	1871.0	0.455

#### 3.2. Model validation

While we have yet to test a receiver using the HFSS, we have validated the COMSOL model of the cup-cone receiver subassembly, comparing it to an assembly constructed for experiment. This validation was obtained by heating the receiver using heating coils. By controlling the coils’ duty cycle and reproducing the heating conditions within COMSOL, we were able to compare simulations of the receiver to experimental data. Since these tests were performed in air, temperatures were kept well below  $300^\circ\text{C}$ , to avoid any oxidation.

Our first validation entailed heating the receiver from ambient temperature to approximately  $220^\circ\text{C}$ , then held at steady-state for approximately 48 h. After this time, the aperture to the receiver was plugged with insulation to eliminate natural convection and radiation through the aperture to the environment, and the receiver was allowed to cool. We also simulated this procedure in COMSOL and compared the results with those obtained experimentally, as shown in Figs. 3 and 4.

For the heat-up portion of the experiment, the discrepancy in final temperature between the experimental and simulation results is 3.9%, which corresponds to a temperature difference of approximately  $8^\circ\text{C}$ . At the end of the simulation ( $\sim 13.5$  h), the difference in predicted and measured temperature was less than  $3^\circ\text{C}$ , which is within the uncertainty associated with the thermocouples used. For comparison, the expected error for the K-type thermocouples used was  $\pm 5^\circ\text{C}$ . The heat

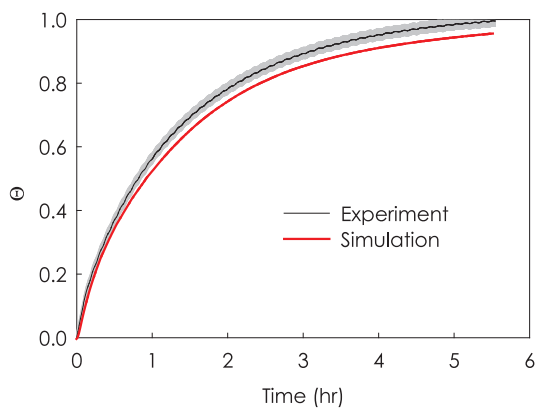


Fig. 3. Experimental and simulation results of the temperature,  $\Theta = \frac{T - T_{amb}}{T_{max} - T_{amb}}$  during a heat-up procedure. Gray shading used to show uncertainty in thermocouple measurement.

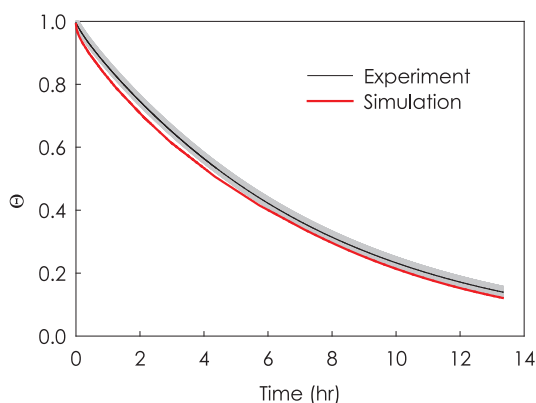


Fig. 4. Experimental and simulation results of the temperature,  $\Theta = \frac{T - T_{amb}}{T_{max} - T_{amb}}$  during a cool-down procedure. Gray shading used to show uncertainty in thermocouple measurement.

capacity of graphite was not measured and is not provided for the AR-14 grade of graphite used for the receiver validation. Instead, we approximated the heat capacity of the graphite based upon the heat capacity of fully dense graphite and the porosity of AR-14. It is also possible that the actual power provided to the heating coils is a few percent lower than stated due to e.g. manufacturing imperfections, oxidation of the coils, or variations in the supplied voltage, or that the effective convective coefficient estimated within the cavity is inaccurate. Nonetheless, despite these discrepancies, the agreement between the model and experiments is good.

To validate the radiation portion of the model, while the receiver was held at its steady-state temperature of 220 °C, we inserted a thermocouple into the cavity and measured the temperature as a function of the depth of insertion. The aperture was not plugged with insulation during this portion of the experiment, nor was it modeled as such when comparing to COMSOL simulations. The results are shown in Fig. 5 and we have included the error bars due to the uncertainty in the readings generated by the thermocouples ( $\pm 5$  °C). The discrepancy between the measured and predicted results can be ascribed in part to neglecting convection within the simulation. We expect convection from the receiver cavity would further heat the thermocouple slightly, which is consistent with the under prediction in Fig. 5. While the temperature does not match perfectly, the correct trend and quantitative capture of the insertion depth where the temperature should change most steeply confirms that the reradiation is being modeled correctly; the data shown in Fig. 5, shows sufficiently good agreement to indicate that the model is sufficiently accurate for the sensitivity study of interest here.

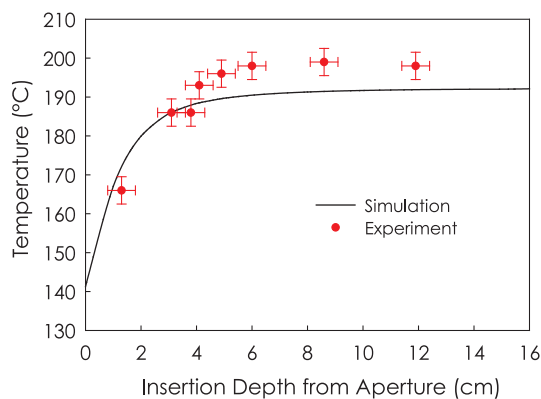


Fig. 5. Experimental measurements and simulation results of cavity temperature at various locations during radiation modeling validation.

### 3.3. Energy balance

Fig. 6 provides a breakdown of the energy balance within the U-tube receiver. Of the 7000 W entering the receiver, 5561 W heat Sn flowing through the receiver, while 62 W are reflected from the cavity (i.e. the energy is never absorbed), 602 W are reradiated from the cavity, 312 W radiate from the surface of the insulation, and 444 W are convected from the insulation surface. These values sum to 6977 W, leaving 23 W (0.33% of the input power) unaccounted for. This discrepancy is due to the coarseness of the mesh used, but is within an acceptable range that still allows the sensitivity to different parameters to be studied.

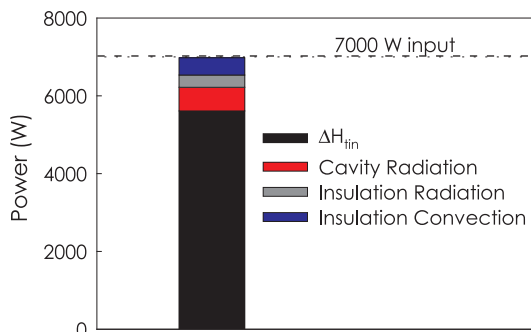


Fig. 6. Assessment of heat losses in the system confirming the energy balance within the simulation domain.

### 3.4. The effect of thermal conductivity

There are two thermal conductivities that were varied in this problem to assess sensitivity, namely the thermal conductivity of the material containing the LMHTF flow, and the material used for the insulation. Because the convective resistance is negligible within the LMHTF, it is not expected that there will be any sensitivity to the LMHTF thermal conductivity for the range associated with liquid metals. Prior to performing this sensitivity analysis however, it was not clear whether the thermal conductivities of other materials available were sufficiently high to enable a high efficiency receiver. In the case of the receiver itself, a material with a low thermal conductivity would not transfer heat efficiently from the irradiated surface to the LMHTF.

To alter the thermal conductivity of materials within the simulations, the temperature dependence of the thermal conductivity for each base case material, namely graphite, and zirconia and microporous insulation, was multiplied by a scaling factor, preserving the temperature dependence of the original material's thermal conductivity. The effective composite thermal conductivity of the insulations used is approximately  $0.05 \text{ W m}^{-1} \text{ K}^{-1}$  (Behar et al., 2013; Bertocchi et al.,

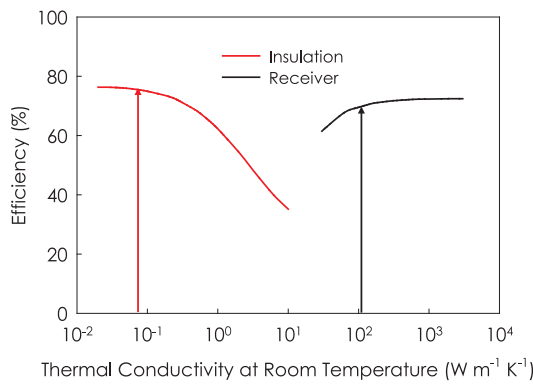


Fig. 7. Receiver efficiency vs. insulation conductivity and graphite conductivity. Actual values for each material being used shown using arrows.

2004), while the thermal conductivity of the graphite is  $\sim 102 \text{ W m}^{-1} \text{ K}^{-1}$  (Cormack et al., 1974) at room temperature. From Fig. 7, as the insulation thermal conductivity increases above  $\sim 0.1 \text{ W m}^{-1} \text{ K}^{-1}$ , the receiver efficiency drops dramatically. It is beneficial that commercially available high temperature insulation can in fact achieve a much lower effective thermal conductivity of  $\sim 0.05 \text{ W m}^{-1} \text{ K}^{-1}$ , which can be achieved by placing microporous insulation in series with fibrous zirconia. However, if the conductivity significantly exceeds this value, heat losses through the insulation can become the primary loss mechanism.

Like the insulation, the thermal conductivity of the base case receiver material (e.g., graphite) sits very near the regime where the efficiency is heavily penalized. Very few refractory materials have a sufficiently high thermal conductivity to enable an efficient receiver while also being chemically compatible with molten Sn; graphite is rather unique in this respect. It is worth noting though that it is quite possible that a somewhat lower thermal conductivity could be tolerated as long as it is higher than graphite at high temperature. For example, certain electrically conductive ceramics such as ZrC might also work, since they would be expected to exhibit much less of a decrease in thermal conductivity at high temperature.

### 3.5. The effect of emissivity

To test the effect of emissivity on receiver performance, emissivity values were altered for both the tube itself and the cavity walls, as depicted in Fig. 8. One of four values was prescribed for each surface independently: 0, 0.45, 0.8, or 1, for a total of 16 different possible combinations of emissivity. The values selected are based on the extreme cases for emissivity (0 or 1), as well as an approximate emissivity for graphite (0.8) (Thorn and Simpson, 1953) and mullite (0.45) (Bauer et al., 2005).

Table 2 gives the efficiency of the U-tube receiver for the 16 different emissivity scenarios and confirms several qualitative trends that were to be expected. When both emissivities are set to exactly zero, no light is absorbed by the receiver, so  $300 \text{ }^\circ\text{C}$  Sn cools as it flows through the receiver, resulting in a negative efficiency. When comparing all other cases, the difference in receiver efficiency is only 5% (absolute) maximum. In these cases, the temperature profile is nearly identical. The lack of sensitivity to the optical properties is instructive, and is a somewhat unexpected insight. Furthermore, altering emissivities at such extreme temperatures and high fluxes is expected to pose a substantial materials challenge. Instead, other properties should take precedence over optimizations focused on optical properties, which is an important insight.

The effect of the insulation emissivity at the surface of the insulation was also considered, but the receiver efficiency is highly insensitive to the insulation emissivity, affecting the efficiency by less than 0.1%, as the thermal resistance provided by the insulation is 1–2 orders of

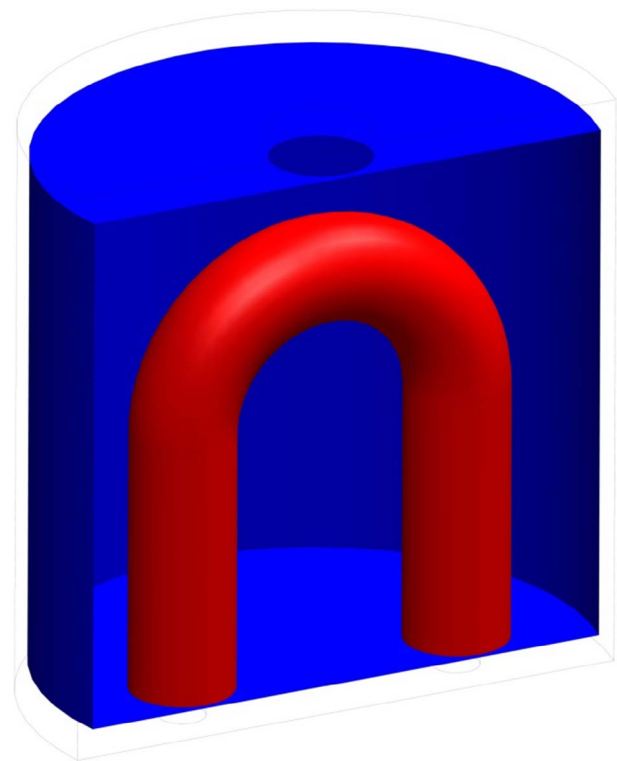


Fig. 8. Illustration of the two different groups of surfaces whose emissivities were altered. The “tube” surfaces are shown in red, while the “cavity walls” surfaces are shown in blue. (For interpretation of the references to color in this figure legend, the reader is referred to the web version of this article.)

Table 2

Receiver efficiency vs. emissivity of the tube and cavity walls. Cell color is based on efficiency, with higher values in green and lower values in red. The negative value shown for the case when all emissivities are set to zero is due to the fact that the receiver cannot absorb any energy, and loses a small amount of heat to losses through the insulation, since the incoming Sn ( $300 \text{ }^\circ\text{C}$ ) is already significantly above ambient.

$\epsilon_{tube}$	$\epsilon_{walls}$			
	1	0.8	0.45	0
1	66.8	67.0	67.6	69.2
0.8	67.5	67.1	67.5	69.4
0.45	66.5	66.5	66.6	67.9
0	65.4	65.1	64.4	-0.2

magnitude higher than resistance due to convection or radiation from the insulation surface.

### 3.6. The effect of convection to the environment

Although reradiation is the primary concern in this sensitivity analysis due its scaling with the fourth power of temperature,

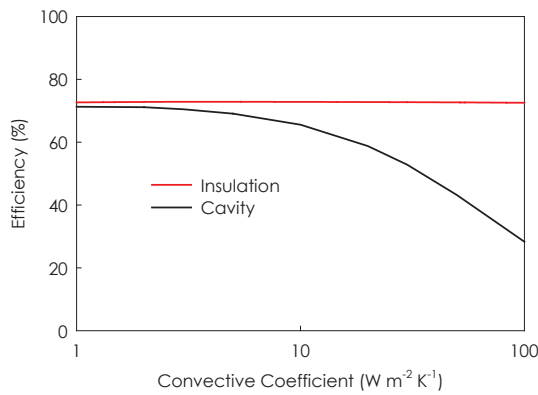


Fig. 9. Receiver efficiency vs. convective coefficient of the cavity surface and the insulation surface.

convection is still an important effect to consider. While the effect of the convective coefficient at the surface of the insulation is insignificant, convection through the aperture from the cavity to the environment can lead to significant heat leakage from the receiver.

For the initial sensitivity analysis, an effective heat transfer coefficient,  $h$ , was prescribed on the receiver surfaces to determine the point at which its value would have a significant effect on the receiver performance. It is clear from Fig. 9 that even for small convective coefficients typical of natural convection (5–10 W m<sup>-2</sup> K<sup>-1</sup>), convection from the cavity can lead to a significant drop in receiver efficiency. At higher coefficients, convection causes the efficiency to decrease drastically. However, since the gas will not be externally forced and will only be driven by buoyancy, the value of  $h$  is likely < 15 W m<sup>-2</sup> K<sup>-1</sup>.

The behavior of buoyancy driven flows within the cavity differs from typical cases discussed in the literature (Balaji and Venkateshan, 1994; Bilgen and Oztop, 2005; Chan and Tien, 1985; Clausing, 1981; Fang et al., 2011; Harris and Lenz, 1985; Hughes and Lovegrove, 2004; Leong et al., 1999; Martyushev and Sheremet, 2014). As the gas properties can vary by factors of more than 3 over the temperature range considered, rendering the calculation of an effective Rayleigh number within the cavity an inaccurate representation of the flow. For reference, the density, kinematic viscosity, thermal expansion coefficient, and thermal diffusivity of nitrogen at 25/1350 °C are: 1.1/0.21 kg m<sup>-3</sup>, 1.6 × 10<sup>-5</sup>/5.3 × 10<sup>-3</sup> kg m<sup>-1</sup> s<sup>-1</sup>, 3.4 × 10<sup>-3</sup>/0.62 × 10<sup>-3</sup> K<sup>-1</sup>, and 2.2 × 10<sup>-5</sup>/0.76 × 10<sup>-5</sup> m<sup>2</sup> s<sup>-1</sup> respectively. Therefore, the local Rayleigh number may vary drastically (more than 500X) between locations. Secondly, the geometry in question is complex, and the heating load on the cavity walls is neither a constant temperature nor constant heat flux. Third, the effective convective coefficient is expected to be strongly dependent on the location of the aperture, i.e. whether it is located at the top or bottom of the receiver, or on one of the sides, as is the case in our assembly. Because of these

irregularities, simple approximations to determine an effective convective coefficient are likely to be inaccurate.

Due to the uniqueness of the problem, accurately determining the gas dynamics necessitates the use of direct numerical solution via computational fluid dynamics (CFD). Given the computational expense required to converge natural convection CFD simulations, cavity convection was not simulated in conjunction with reradiation, heat conduction, and fluid flow. Instead, the effective value for the convective heat transfer coefficient was studied for the final cup-cone geometry, using a prescribed temperature distribution for the cavity walls, determined by first simulating all other heat transfer mechanisms and assuming a nominal value 5 W m<sup>-2</sup> K<sup>-1</sup> for the convective heat transfer coefficient. The resulting temperature profile was then used to study the natural convective flow, which then allowed for calculation of the natural convective heat transfer coefficient. The sensitivity to the effective cavity convection coefficient is shown in Fig. 9 and illustrates that it is likely one of the most important parameters that can affect the efficiency, given that an effective value in the range 1–15 W m<sup>-2</sup> K<sup>-1</sup> is expected.

To generate an estimate of the nominal convective coefficient, the flow of gas occupying both the volume within cavity and the space immediately outside the cavity was simulated for the cup-cone geometry. Eqs. (3) and (5), (6) were applied to nitrogen, which occupied the volume within the cavity as well as the volume near the cavity aperture (see Fig. 10). An additional term was added to Eq. (4) to account for gravity:

$$\frac{\partial(u_i \rho u_j)}{\partial x_i} = -\frac{\partial p}{\partial x_i} + \frac{\partial}{\partial x_i} \left( \mu \frac{\partial u_j}{\partial x_i} \right) + \rho g \quad (11)$$

Boundary conditions were prescribed by setting the temperature at each surface equal to the temperature generated by previous thermal modeling of the receiver, when a prescribed convective coefficient of 5 W m<sup>-2</sup> K<sup>-1</sup> was used. At the boundary open to the environment, the gauge pressure of the gas was set equal to zero and the temperature to 25 °C. From the CFD simulations, the resultant convective heat flux is approximately 370 W, which corresponds to an effective heat transfer coefficient of 4.47 W m<sup>-2</sup> K<sup>-1</sup> on the inner surfaces of the receiver, where  $Q = hA_s(T - T_{inf})$ , (that is, direct convection from the receiver surfaces to the ambient gas environment).

Cross-sections of the gas temperature and velocity are given in Fig. 10. N<sub>2</sub> within the cavity is nearly stagnant, leading to hot gases trapped within the cavity. N<sub>2</sub> at ~800 °C flows out of the top of the aperture, while ambient temperature N<sub>2</sub> flows into the bottom. Although cavity convection can be a significant heat loss, there are strategies to potentially combat it, particularly if one uses an external flow to trap the hot gasses inside the receiver, often termed an “air curtain” (Chen et al., 2012; Hayes and Stoecker, 1969a, 1969b).

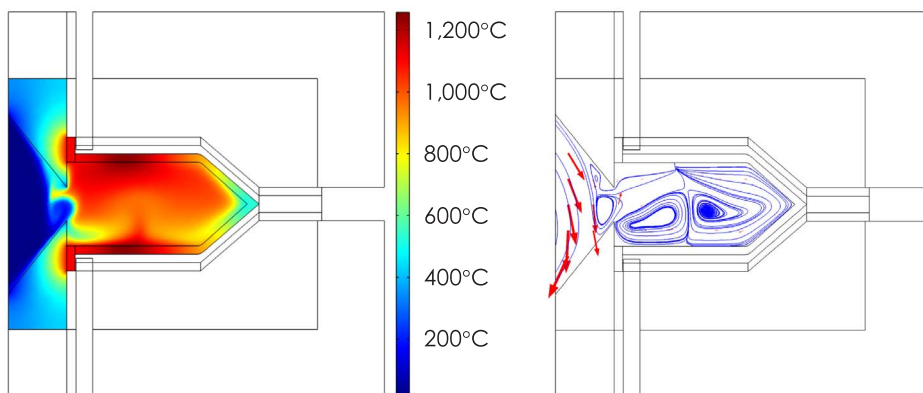


Fig. 10. Temperature map of the gas within the receiver as well as solid bodies with which it is in direct contact (left) and velocity profile of gas within the cavity (right). Velocity magnitude shown using red arrows, and streamlines in blue. Gravity acts downwards. (For interpretation of the references to color in this figure legend, the reader is referred to the web version of this article.)

### 3.7. The importance of hot spot location

Because radiation scales with  $T^4$ , minimizing the view factor between the hottest portions of the receiver and the aperture can significantly reduce reradiative losses. However, the hottest portions are generally those with a high view factor back to the aperture, as portions of the receiver with a high view factor to the aperture typically also absorb a high fraction of the incoming light. Though a hot spot with a high view factor to the aperture will result in increased losses due to reradiation from the cavity, a hotspot close to the exit point of the Sn allows the Sn to be heated locally above temperatures achieved in the rest of the receiver. Thus, an optimal receiver geometry should be designed in such a way that locates hot spots near the Sn outlets but with a low view factor to the receiver aperture. Here, it should be emphasized that is useful to think about the receiver in terms of a local energy balance, with incident light on one face, reradiation back out from the same face, and conduction to the liquid metal on the back face. From this viewpoint, it becomes clear that the incident light must exceed the local reradiation in order for the liquid metal to be heated. Otherwise, the liquid metal will locally be cooled. Given the fourth power scaling of the reradiation, this then necessitates non-uniform flux in the receiver, since the locations where the liquid metal is hottest need much higher incidence to overcome the local reradiative losses and continue heating the LMHTF. The need for a hot spot in such a high temperature receiver is an interesting new insight that was not obvious at first.

For the receiver geometries studied herein, the effective blackbody temperature of the cavity (calculated based on the flux of reradiation through the aperture) is typically 1000–1100 °C, even though the peak temperature is 1350 °C. For the cup-cone receiver geometry, heating Sn from 300 °C to 1350 °C, the reradiation is less than half that of a cavity that is uniformly at 1350 °C, corresponding to an effective cavity blackbody temperature of 981 °C. This result is important, because it suggests that one can use geometry to significantly suppress reradiative losses. Referring back to Eq. (2), setting the nominal blackbody temperature of the receiver equal to the peak temperature is therefore a poor approximation, as reradiation from the cavity can be suppressed significantly below this limit. Exploiting this effect could be crucial towards achieving a design that can reach ~90% efficiency at ~1350 °C. Thus, the hot spot location and its effect on receiver efficiency is an important effect to be explored in a future design optimization study.

### 3.8. The importance of thermal stresses

As mentioned previously, thermal stresses are one of the most important factors to consider when developing a receiver geometry at the laboratory scale. With receiver dimensions on the order of 30 cm and the temperature difference within the receiver ~1000 °C, temperature gradients in the receiver are expected to be 50–100 °C/cm. Such gradients may result in stresses that exceed graphite’s fracture strength. Furthermore, in many of the initial geometries examined, this temperature gradient is compounded by the existence of sharp features that

**Table 3**  
Maximum stress developed in both receiver geometries. Efficiency of each receiver is also provided.

Geometry	Maximum stress (MPa)	Efficiency (%)
U-Tube	325	67.1
Cup-cone	10.8	83.3

can act as stress concentrators.

Due to the number of other factors investigated, thermal stresses were not initially considered when designing receiver geometries; initially, only the thermal performance of the receiver was considered, in order to determine which heat loss mechanisms were most impactful on its efficiency. Once these factors had been quantified, stresses within the receivers were subsequently examined. The first principle stress profile, determined from Eq. (10), are shown for both receivers in Fig. 11. The maximum stress developed in both the U-tube and cup-cone geometries is given in Table 3.

Many aspects of the cup-cone receiver are designed to minimize thermal stresses. Specifically, the tapered inlet was added and reduces thermal stresses near the inlet by an order of magnitude. Stresses due to the local hot spot/ring that forms near the aperture (visible for the U-tube receiver) are managed by using a “lid” made of insulation, which can tolerate the extreme temperature gradients at the hot spot. Additionally, utilizing graphite near the aperture leads to additional heat spreading away from the hotspot formed at the aperture, increasing thermal losses, which further motivates the use of insulation to create the aperture.

The maximum stress expected in the cup-cone design is only 10.8 MPa. The fracture strength of the AR-14 graphite, from which an experimental receiver has been fabricated, is 43 MPa, which is 4.0 times the maximum stress developed in the cup-cone receiver. Thus, the receiver is not expected to fail during testing, with a factor of safety of 4. Furthermore, fatigue is generally not a concern for graphite, particularly when stresses remain below half the fracture strength of graphite (Leichter and Robinson, 1970), and graphite does not creep significantly, even at 1400 °C (Blackstone, 1977). Thus, it is not anticipated that either of these issues will cause a failure during an experimental test of the cup-cone receiver.

### 3.9. Summary of efficiency sensitivity

The importance of the various parameters/effects studied herein are ranked in Table 4 below, from most to least impactful. Also included is the minimum impact each parameter has on efficiency, assuming the receiver is well-designed to minimize losses associated with that parameter.

While many of these parameters have a significant effect on efficiency, none of them are impactful enough to preclude realization of a high-efficiency receiver. Considering that graphite provides sufficiently high thermal conductivity and commercially available high temperature insulation has a low enough effective thermal conductivity to

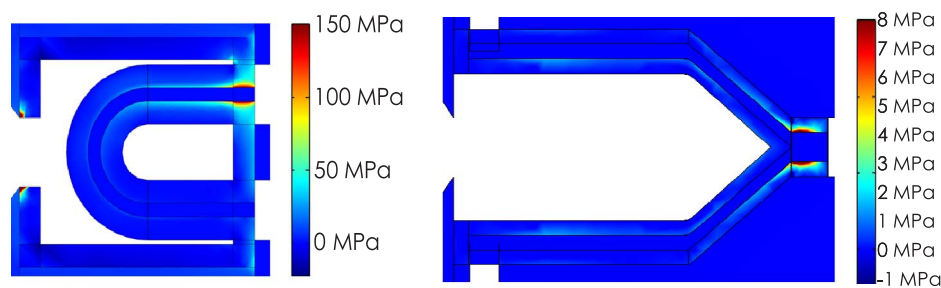


**Fig. 11.** First principle stress profile of the U-tube and cup-cone receivers. Positive values indicate tensile stresses, while negative values indicate compressive stresses. Note here the difference between the range in stresses for the two receivers. Fixations are on the cold side of the insulation (not pictured), which was in turn allowed to deform freely.

**Table 4**

List of various receiver parameters, the extent to which they affect the total receiver efficiency, and the effect each has on efficiency if the receiver is designed taking these factors into account.

Parameter	Nominal sensitivity (% of efficiency)	Minimum sensitivity (% of efficiency)
Insulation thermal conductivity	20–30%	~5%
Cavity thermal conductivity	10–15%	~5%
LMHTF mass flowrate	~15%	N/A <sup>a</sup>
Convection off cavity surfaces	~10%	~5%
Radiation from cavity	5–10%	~5%
Insulation thickness	~5%	< < 1%
Cavity dimensions	~5%	~1%
Cavity emissivity	< 5%	~1%
Convection off insulation surface	< 1%	< < 1%
Radiation from insulation surfaces	< 1%	< < 1%

<sup>a</sup> Mass flowrate is determined by the target outlet temperature, thus the receiver cannot be designed to improve efficiency based on altering the mass flowrate.

impart a negligibly small penalty, the three predominant losses (e.g., reradiation, heat leakage through the insulation, and cavity convection) can potentially be reduced to ~10% overall. This finding suggests that doing so requires incident fluxes above  $2500 \text{ kW m}^{-2}$  and reduced cavity convection through the usage an effective air curtain (Chen et al., 2012; Hayes and Stoecker, 1969a, 1969b), resulting in a ~90% efficient receiver. Furthermore, there exists additional opportunities to reduce losses further at utility-scale. For example, losses from the surface of the insulation are expected to decrease, as the ratio of surface area to volume decreases at larger scales. Furthermore, a single receiver would not be expected to traverse the entire temperature difference. Instead, one would likely use an array of smaller modular receivers each of which would experience a small portion of the total temperature difference. Doing so allows one to further reduce reradiative losses by positioning the receiver modules that experience the peak temperatures in the region where the peak flux incident from heliostats is maximized, with a reduced acceptance angle to enable higher concentration. Thus, the full receiver efficiency would become some effective average of individual receiver module efficiencies and lower temperature receiver modules can be designed to greatly exceed 90% efficiency.

#### 4. Conclusion

Several factors were found to have a strong effect on the performance of cavity receivers, while others had little to no effect. Cavity dimensions, insulation thickness, modes of heat transfer at the surface of the insulation (i.e. convection and reradiation), and the emissivity of the inner cavity surface were all shown to have little to no effect on the receiver efficiency. On the other hand, the thermal conductivity of materials used in the receiver, as well as convection from the receiver cavity and the location of hot spots within the receiver can significantly impact receiver efficiency. Although it does not directly impact receiver efficiency, another factor to consider is the thermal stresses developed in the receiver, because they can determine reliability and the likelihood of thermo-mechanical failure. However, various strategies can be employed to minimize these stresses, including the elimination of sharp features, tapering the inlet region of the receiver, and creating a receiver “lid” made of insulation rather than graphite. It is evident that with careful engineering, it is possible to construct a high-temperature receiver that can attain efficiencies  $\geq 80\%$  and possibly  $\geq 90\%$ , particularly if the receiver were scaled up to utility-scale. The fact that the results herein suggest such a high receiver efficiency is possible bolsters

the general feasibility of using a LMHTF in for CSP, particularly since the materials exist and are compatible that could allow such a technology to exist. While joining graphite has proven to be a challenge at the laboratory scale, we have successfully utilized mechanical joints (e.g. threaded graphite tubes) and graphite “glues”, to seal our piping network against leaks. Additional information may be found in (Amy et al., 2017). Furthermore, the recent demonstration of high temperature infrastructural components to pump and continuously circulate liquid tin above  $1000 \text{ }^\circ\text{C}$  (Amy et al., 2017), also suggest this is a potentially feasible pathway for CSP. Additional work is necessary to demonstrate this feasibility of receiver subsystems and eventually full systems (Amy et al., 2017), but this initial sensitivity study sheds light on the most important variables to be considered towards the design of a highly efficient, high temperature receiver.

#### Acknowledgment

This work was supported by the Advanced Research Projects Agency – Energy, Project No. DE-AR0000339; and the National Science Foundation Graduate Research Fellowship under Grant No. DGE-1148903.

#### References

- Balaji, C., Venkateshan, S., 1994. Correlations for free convection and surface radiation in a square cavity. *Int. J. Heat Fluid Flow* 15 (3), 249–251.
- Bauer, W., Moldenhauer, A., Platzer, A., 2005. Emissivities of ceramic materials for high temperature processes. In: *Optics & Photonics 2005*. International Society for Optics and Photonics, pp. 58800W–58800W-58810.
- Becker, M., Fend, T., Hoffschmidt, B., Pitz-Paal, R., Reutter, O., Stamatov, V., Steven, M., Trimis, D., 2006. Theoretical and numerical investigation of flow stability in porous materials applied as volumetric solar receivers. *Sol. Energy* 80 (10), 1241–1248.
- Behar, O., Khellaf, A., Mohammedi, K., 2013. A review of studies on central receiver solar thermal power plants. *Renew. Sustain. Energy Rev.* 23, 12–39.
- Bergman, T.L., Incropera, F.P., Lavine, A.S., 2011. *Fundamentals of Heat and Mass Transfer*. John Wiley & Sons.
- Bertocchi, R., 2002. Carbon particle cloud generation for a solar particle receiver. *J. Sol. Energy Eng.* 124 (3), 230–236.
- Bertocchi, R., Karni, J., Kribus, A., 2004. Experimental evaluation of a non-isothermal high temperature solar particle receiver. *Energy* 29 (5), 687–700.
- Bilgen, E., Oztop, H., 2005. Natural convection heat transfer in partially open inclined square cavities. *Int. J. Heat Mass Transf.* 48 (8), 1470–1479.
- Blackstone, R., 1977. Radiation creep of graphite. An introduction. *J. Nucl. Mater.* 65, 72–78.
- Bradshaw, R., Meeker, D., 1990. High-temperature stability of ternary nitrate molten salts for solar thermal energy systems. *Sol. Energy Mater.* 21 (1), 51–60.
- Bradshaw, R.W., Siegel, N.P., 2008. Molten nitrate salt development for thermal energy storage in parabolic trough solar power systems. In: *ASME 2008 2nd International Conference on Energy Sustainability collocated with the Heat Transfer, Fluids Engineering, and 3rd Energy Nanotechnology Conferences*. American Society of Mechanical Engineers, pp. 631–637.
- Branz, H.M., Regan, W., Gerst, K.J., Borak, J.B., Santori, E.A., 2015. Hybrid solar converters for maximum exergy and inexpensive dispatchable electricity. *Energy Environ. Sci.* 8 (11), 3083–3091.
- Bugge, J., Kjær, S., Blum, R., 2006. High-efficiency coal-fired power plants development and perspectives. *Energy* 31 (10), 1437–1445.
- Amy, C., Budenstein, D., Bagepalli, M., England, D., DeAngelis, F., Wilk, G., Jarrett, C., Kelsall, C., Hirschey, J., Wen, H., Chavan, A., Gilleland, B., Yuan, C., Chueh, W., Sandhage, K.H., Kawajiri, Y., Henry, A., 2017. Pumping liquid metal at high temperatures up to 1673 kelvin. *Nature* 550 (7675), 199–203.
- Cable, R., Blake, K.O.C.D., Nrel, H.P., Petrovitz, N., 2003. Overview on use of a Molten Salt HTF in a trough solar field.
- Chan, Y., Tien, C., 1985. A numerical study of two-dimensional laminar natural convection in shallow open cavities. *Int. J. Heat Mass Transf.* 28 (3), 603–612.
- Chen, F., Wittkopf, S.K., Ng, P.K., Du, H., 2012. Solar heat gain coefficient measurement of semi-transparent photovoltaic modules with indoor calorimetric hot box and solar simulator. *Energy Build.* 53, 74–84.
- Clausing, A., 1981. An analysis of convective losses from cavity solar central receivers. *Sol. Energy* 27 (4), 295–300.
- Cormack, D., Leal, L., Imberger, J., 1974. Natural convection in a shallow cavity with differentially heated end walls. Part 1. Asymptotic theory. *J. Fluid Mech.* 65 (02), 209–229.
- Denholm, P., Clark, K., O’Connell, M., 2016. On the path to SunShot: emerging issues and challenges in integrating high levels of solar into the electrical generation and transmission system. NREL (National Renewable Energy Laboratory (NREL), Golden, CO (United States)).
- Denholm, P., Jorgenson, J., Hummon, M., Jenkin, T., Palchak, D., Kirby, B., Ma, O., O’Malley, M., 2013. The value of energy storage for grid applications. *Contract* 303,

- 275–3000.
- Denholm, P., Mehos, M., 2014. Enabling greater penetration of solar power via the use of CSP with thermal energy storage. *Sol. Energy: Appl., Econ., Pub. Percept.*, 99.
- Donohoo-Vallett, P., 2016. RevolutionEllipsis Now. The Future Arrives for Five Clean Energy Technologies – 2016 Update. In: Energy, D.O. (Ed.).
- EIA, U., 2013. Updated capital cost estimates for utility scale electricity generating plants. *US Energy Inf. Adm.*
- Fang, J.-B., Wei, J.-J., Dong, X.-W., Wang, Y., 2011. Thermal performance simulation of a solar cavity receiver under windy conditions. *Sol. Energy* 85 (1), 126–138.
- Fernandez, A., Lasanta, M., Perez, F., 2012. Molten salt corrosion of stainless steels and low-Cr steel in CSP plants. *Oxid. Met.* 78 (5–6), 329–348.
- Garcia-Casals, X., Ajona, J.I., 1999. The duct selective volumetric receiver: potential for different selectivity strategies and stability issues. *Sol. Energy* 67 (4), 265–286.
- Goods, S., Bradshaw, R.W., 2004. Corrosion of stainless steels and carbon steel by molten mixtures of commercial nitrate salts. *J. Mater. Eng. Perform.* 13 (1), 78–87.
- Harris, J.A., Lenz, T.G., 1985. Thermal performance of solar concentrator/cavity receiver systems. *Sol. Energy* 34 (2), 135–142.
- Hayes, F., Stoecker, W., 1969a. Design data for air curtains. *Ashrae Trans.* 75 (2), 168–180.
- Hayes, F., Stoecker, W., 1969b. Heat transfer characteristics of the air curtain. *ASHRAE Trans.* 75 (2), 153–167.
- Hughes, G., Lovegrove, K., 2004. Experimental investigation of natural convection heat loss from a model solar concentrator cavity receiver.
- Karni, J., Kribus, A., Doron, P., Rubin, R., Fiterman, A., Sagie, D., 1997. The DIAPR: a high-pressure, high-temperature solar receiver. *J. Sol. Energy Eng.* 119 (1), 74–78.
- Karni, J., Kribus, A., Rubin, R., Doron, P., 1998. The “porcupine”: a novel high-flux absorber for volumetric solar receivers. *J. Sol. Energy Eng.* 120 (2), 85–95.
- Kribus, A., Doron, P., Rubin, R., Karni, J., Reuven, R., Duchan, S., Taragan, E., 1999. A multistage solar receiver: the route to high temperature. *Sol. Energy* 67 (1), 3–11.
- Krueger, K.R., 2012. Design and Characterization of a Concentrating Solar Simulator. University of Minnesota.
- Kruizenga, A., Gill, D., 2014. Corrosion of iron stainless steels in molten nitrate salt. *Energy Proc.* 49, 878–887.
- Leichter, H., Robinson, E., 1970. Fatigue behavior of a high-density graphite and general design correlation. *J. Am. Ceram. Soc.* 53 (4), 197–204.
- Leong, W., Hollands, K., Brunger, A., 1999. Experimental Nusselt numbers for a cubical-cavity benchmark problem in natural convection. *Int. J. Heat Mass Transf.* 42 (11), 1979–1989.
- Margolis, R., Coggeshall, C., Zuboy, J., 2012. SunShot Vision Study. US Dept. of Energy.
- Martyushev, S.G., Sheremet, M.A., 2014. Conjugate natural convection combined with surface thermal radiation in an air filled cavity with internal heat source. *Int. J. Therm. Sci.* 76, 51–67.
- NREL, 2016. Crescent Dunes Solar Energy Project. <[https://www.nrel.gov/csp/solarpaces/project\\_detail.cfm/projectID=60](https://www.nrel.gov/csp/solarpaces/project_detail.cfm/projectID=60)> (accessed 1/23/2017).
- Pachauri, R.K., Allen, M., Barros, V., Broome, J., Cramer, W., Christ, R., Church, J., Clarke, L., Dahe, Q., Dasgupta, P., 2014. Climate Change 2014: Synthesis Report. Contribution of Working Groups I, II and III to the Fifth Assessment Report of the Intergovernmental Panel on Climate Change.
- Pacio, J., Wetzel, T., 2013. Assessment of liquid metal technology status and research paths for their use as efficient heat transfer fluids in solar central receiver systems. *Sol. Energy* 93, 11–22.
- Pitz-Paal, R., Dersch, J.r., Milow, B., T ellez, F.I., Ferriere, A., Langnickel, U., Steinfeld, A., Karni, J., Zarza, E., Popel, O., 2005. Development steps for concentrating solar power technologies with maximum impact on cost reduction: results of the European ECOSTAR study. ASME 2005 International Solar Energy Conference. American Society of Mechanical Engineers, pp. 773–779.
- Pitz-Paal, R., Hoffschmidt, B., B ohmer, M., Becker, M., 1997. Experimental and numerical evaluation of the performance and flow stability of different types of open volumetric absorbers under non-homogeneous irradiation. *Sol. Energy* 60 (3), 135–150.
- Ries, H., Segal, A., Karni, J., 1997. Extracting concentrated guided light. *Appl. Opt.* 36 (13), 2869–2874.
- Ries, H., Spirkel, W., 1996. Inherent limitations of volumetric solar receivers. *J. Sol. Energy Eng.* 118, 151.
- Rolf, B., Henrik, N., Judy, W., 1999. Combined-cycle Gas and Steam Turbine Power Plants.
- Rose, A., 1985. Calculation of critical stress intensity factors of nuclear graphite from small specimen tests. *Carbon* 23 (4), 387–393.
- Siegel, N.P., Ho, C.K., Khalsa, S.S., Kolb, G.J., 2010. Development and evaluation of a prototype solid particle receiver: on-sun testing and model validation. *J. Sol. Energy Eng.* 132 (2), 021008.
- Sioshansi, R., Madaeni, S.H., Denholm, P., 2014. A dynamic programming approach to estimate the capacity value of energy storage. *IEEE Trans. Power Syst.* 29 (1), 395–403.
- Steinfeld, A., 2002. Solar hydrogen production via a two-step water-splitting thermochemical cycle based on Zn/ZnO redox reactions. *Int. J. Hydrogen Energy* 27 (6), 611–619.
- Stewart, M., Weinberg, F., 1972. Fluid flow in liquid metals: I. Theoretical analysis. *J. Cryst. Growth* 12 (3), 217–227.
- Tanaka, H., Sawai, S., Morimoto, K., Hisano, K., 2001. Measurement of spectral emissivity and thermal conductivity of zirconia by thermal radiation calorimetry. *J. Therm. Anal. Calorim.* 64 (3), 867–872.
- Thorn, R., Simpson, O., 1953. Spectral emissivities of graphite and carbon. *J. Appl. Phys.* 24 (5), 633–639.
- Wang, F., Cheng, L., Mei, H., Zhang, Q., Zhang, L., 2014. Effect of surface microstructures on the infrared emissivity of graphite. *Int. J. Thermophys.* 35 (1), 62–75.
- Weitzel, P.S., 2011. Steam generator for advanced ultra supercritical power plants 700 C to 760 C. ASME 2011 Power Conference Collocated with JSME ICOPE 2011. American Society of Mechanical Engineers 281–291.
- Wilk, G., 2016. Liquid Metal Based High Temperature Concentrated Solar Power: Cost Considerations.
- Wolff, F., Beckermann, C., Viskanta, R., 1988. Natural convection of liquid metals in vertical cavities. *Exp. Therm Fluid Sci.* 1 (1), 83–91.
- Wright, I., Maziasz, P., Ellis, F., Gibbons, T., Woodford, D., 2004. Materials issues for turbines for operation in ultra-supercritical steam. Research Sponsored by the US Department of Energy, Office of Fossil Energy, Advanced Research Materials Program, Under Contract DE-AC05-00OR22725 with UT-Battelle LLC.
- Zhang, Y., Cai, Y., Hwang, S., Wilk, G., DeAngelis, F., Henry, A., Sandhage, K., 2018. Containment materials for liquid tin at 1350 °C as a heat transfer fluid for high temperature concentrated solar power. *Sol. Energy* (in print).
- Yang, Z., Garimella, S.V., 2010. Thermal analysis of solar thermal energy storage in a molten-salt thermocone. *Sol. Energy* 84 (6), 974–985.